

1 ***Engineering Phosphatidylinositol-4,5-bisphosphate model membranes enriched***
2 ***in endocytic cargo: a neutron reflectometry, AFM and QCM-D structural study***

3

4 **Daniel Pereira** ^{1,2,a}, **Andreas Santamaria** ^{2,3,a}, **Nisha Pawar** ⁴, **Javier Carrascosa-**
5 **Tejedor** ^{2,5}, **Mariana Sardo** ¹, **Luís Mafra** ¹, **Eduardo Guzmán** ^{3,6}, **David J. Owen** ⁷,
6 **Nathan R. Zaccai** ⁷, **Armando Maestro** ^{8,9,*}, **Ildefonso Marín-Montesinos** ^{1,*}

7

8 1 Department of Chemistry, CICECO, University of Aveiro, 3810-193, Aveiro, Portugal

9 2 Large Scale Structures Group, Institut Laue-Langevin, 38042 Cedex 9, Grenoble, France

10 3 Departamento de Química Física, Universidad Complutense de Madrid, 28040, Madrid, Spain

11 4 Centro de Física de Materiales (CSIC, UPV/EHU) - Materials Physics Center MPC, Paseo Manuel de
12 Lardizabal 5, E-20018 San Sebastián, Spain.

13 5 Division of Pharmacy and Optometry, University of Manchester, M13 9PT, Manchester, UK

14 6 Instituto Pluridisciplinar, Universidad Complutense de Madrid, 28040 Madrid, Spain

15 7 Cambridge Institute for Medical Research, University of Cambridge, CB22 7QQ, Cambridge, UK

16 8 Centro de Física de Materiales (CSIC, UPV/EHU) - Materials Physics Center MPC, Paseo Manuel de
17 Lardizabal 5, E-20018 San Sebastián, Spain.

18 9 IKERBASQUE—Basque Foundation for Science, Plaza Euskadi 5, Bilbao, 48009 Spain

19

20 *Corresponding authors: armando.maestro@ehu.eus (A.M.), imarin@ua.pt (I.M.-M.)

21 ^a Both authors contributed equally to this work.

22 This main manuscript (Manuscript_MainText_ColSB.docx) contains **31 pages** and **8444 words** including
23 titles, list of authors, affiliation, captions, acknowledgments and references. In addition, the present manu-
24 script contains **5 figures**. The supporting information document (Manuscript_SI_ColSB.docx) is composed
25 of **13 pages**, **1122 words**, **6 figures** and **5 tables**.

26

27 **Abstract:**

28 The combination of *in vitro* models of biological membranes based on solid-supported
29 lipid bilayers (SLBs) and of surface sensitive techniques, such as neutron reflectometry
30 (NR), atomic force microscopy (AFM) and quartz crystal microbalance with dissipation

31 monitoring (QCM-D), is well suited to provide quantitative information about molecular
32 level interactions and lipid spatial distributions. In this work, cellular plasma membranes
33 have been mimicked by designing complex SLB, containing phosphatidylinositol 4,5-
34 bisphosphate (PtdIns4,5P₂) lipids as well as incorporating synthetic lipo-peptides that
35 simulate the cytoplasmic tails of transmembrane proteins. The QCM-D results revealed
36 that the adsorption and fusion kinetics of PtdIns4,5P₂ are highly dependent of Mg²⁺. Ad-
37 ditionally, it was shown that increasing concentrations of PtdIns4,5P₂ leads to the for-
38 mation of SLBs with higher homogeneity. The presence of PtdIns4,5P₂ clusters was vis-
39 ualized by AFM. NR provided important insights about the structural organization of the
40 various components within the SLB, highlighting that the leaflet symmetry of these SLBs
41 is broken by the presence of CD4-derived cargo peptides. Finally, we foresee our study
42 to be a starting point for more sophisticated *in vitro* models of biological membranes with
43 the incorporation of inositol phospholipids and synthetic endocytic motifs.

44
45 **Keywords:** Neutron Reflectometry; Quartz Crystal Microbalance with dissipation moni-
46 toring; membrane biomimetics.

47

48 **Introduction**

49

50 The plasma membrane (PM) is a crucial interface between a eukaryotic cell and
51 its surrounding environment. Its role is governed not only by its associated proteins, but
52 also by membrane-specific lipids, such as the phospholipid phosphatidylinositol 4,5-
53 bisphosphate (PtdIns4,5P₂). This phosphoinositide is directly involved in mediating di-
54 verse processes such as cell migration and signalling, gating of ion channels, signal
55 transduction as well as membrane and vesicular trafficking^{1,2}. In particular, the presence
56 of PtdIns4,5P₂ on the inner leaflet of the PM is essential for clathrin-mediated endocyto-
57 sis (CME). Its phosphorylated inositol ring mediates the recruitment to the PM of CME
58 adaptor proteins, like CALM and AP2. These adaptor proteins also specifically bind to

59 PM-associated transmembrane proteins (termed cargos), and drive the formation of
60 clathrin-coated vesicles that transport these cargos to endosomes, the cell's major sort-
61 ing station ^{3,4}.

62 The AP2, the adaptor protein complex is able to bind dileucine-based (D/ExxxLL)
63 and tyrosine-based (YxxΦ) cargo motifs, which are both widely found in transmembrane
64 proteins at the PM. Due to their short and unstructured nature, the endocytic motifs' bio-
65 logical function has been investigated by using short synthetic peptides, either in solu-
66 tion, or associated to lipids membranes as lipo-peptides ⁵⁻⁷.

67 Here, we report an *in vitro* model of the PM based on solid-supported lipid bilayers
68 (SLBs), deposited onto a solid substrate ^{8,9} enriched in both PtdIns4,5P₂ and a lipo-pep-
69 tide containing the dileucine motif from the T-cell surface antigen protein CD4. The po-
70 sition of the peptide moiety mimicked the anchoring point on the PM by which CME could
71 be initiated. The model SLBs' were characterized by neutron reflectometry (NR), atomic
72 force microscopy (AFM) and quartz-crystal microbalance with dissipation monitoring
73 (QCM-D). These techniques have proven to be powerful methods to study the formation
74 and structural organization of similar model membranes ⁹⁻¹¹. While QCM-D can be used
75 to monitor real time formation of bilayers ¹¹⁻¹³ (in variable conditions *e.g.* buffer compo-
76 sition ¹⁴⁻¹⁶ and temperature ¹⁷) and its interaction with proteins ^{18,19}, small molecules ^{20,21}
77 and even DNA ^{22,23}, NR can be used for the structural study of planar biomimetic mem-
78 branes under physiological conditions with sub-nanometric resolution in the direction
79 perpendicular to the plane of the membrane ^{9,24}. In addition, AFM is very useful to visu-
80 alize the in-plane surface coverage as well as the lipids distribution on the solid/liquid
81 interface ²⁵.

82 Given the importance of PtdIns4,5P₂ docking sites for protein recruitment, and
83 the likely influence of the CD4 on membrane-protein interactions, we focus here in sev-
84 eral key aspects of PtdIns4,5P₂-SLBs formation such as the fusion kinetic dependence
85 on both the presence of divalent cations interacting with the inositol ring and the concen-
86 tration of PtdIns4,5P₂. Further analysis of the NR, AFM and QCM-D data, help to

87 elucidate the SLBs structure and composition perpendicular to the plane of the mem-
88 brane, as well as their mechanical properties. Finally, the coplanarity found for CD4 pol-
89 ypeptide random chains and the phosphoinositol rings was discussed in terms of a plau-
90 sible electrostatic interaction between both components.

91

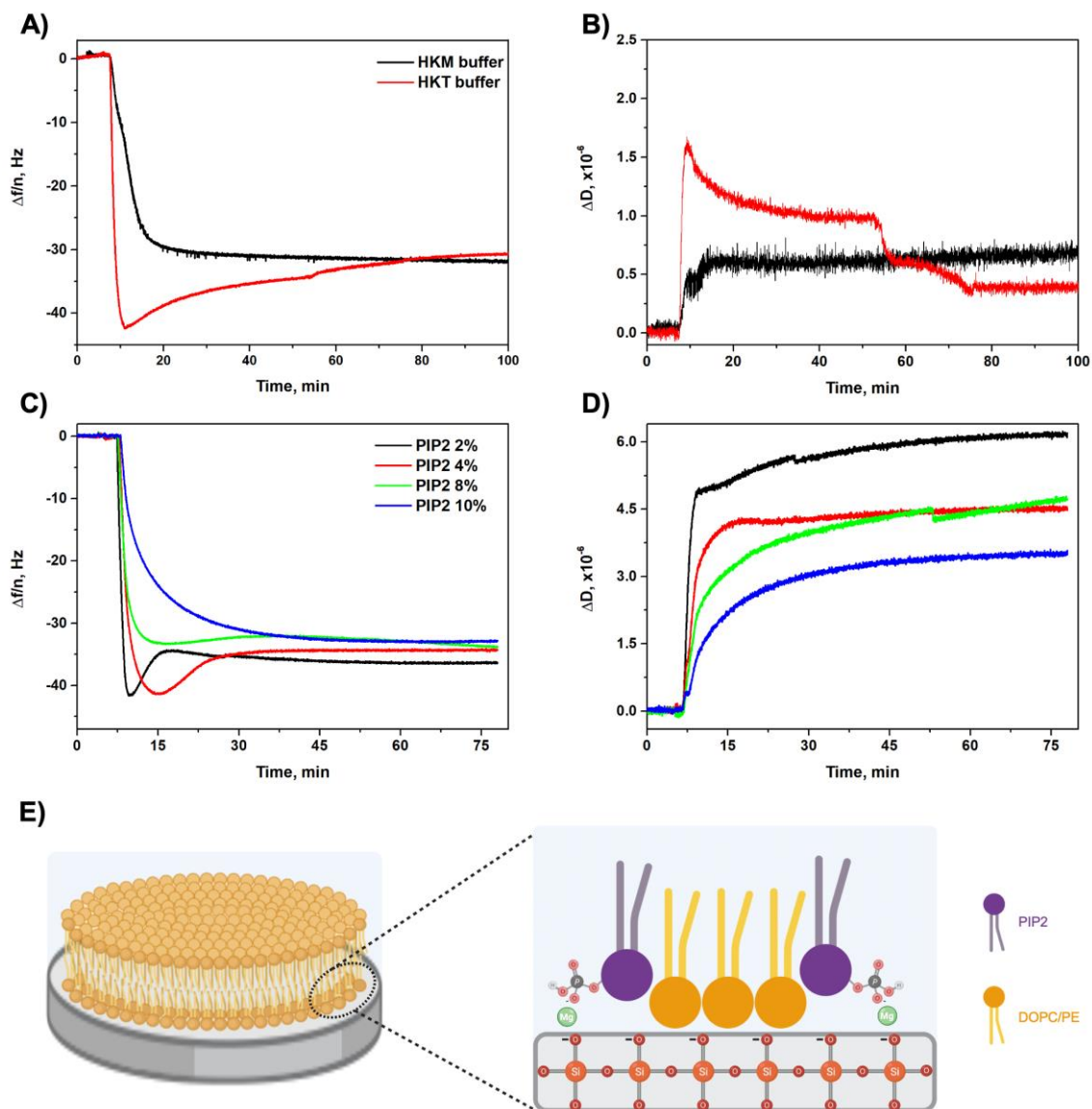
92 **Results and discussion**

93

94 **Effect of divalent cations on vesicle adsorption and fusion kinetics of PtdIns4,5P₂** 95 **enriched SLBs**

96 The formation of SLBs, by liposome adsorption and fusion onto a solid substrate,
97 is highly sensitive to experimental conditions. Vesicle size and concentration, lipid com-
98 position, the buffer pH, ionic type and strength, temperature and substrate type influence
99 both the adsorption and fusion mechanisms^{8,11}. The adsorption and fusion kinetics of
100 (7:2:1) DOPC:DOPE:PtdIns4,5P₂ liposomes were analyzed by QCM-D (see **Methods**
101 for liposomes preparation and characterization).

102 The time evolution of the frequency ($\Delta f/n$, where n is the overtone number) and
103 dissipation (ΔD) shifts, for the 3rd overtone ($n=3$), monitored during the formation of the
104 SLBs on the substrate surface are reported in **Figure 1A, B**.



105

106 **Figure 1:** Vesicle adsorption and fusion kinetics: frequency shift (A) and dissipation shift
 107 (B) plots corresponding to the 3rd overtone ($n=3$) for lipid vesicles composed of DOPC,
 108 DOPE and PtdIns4,5P₂ (in molar ratio 7:2:1), prepared with HKM (5 mM Mg²⁺, black line)
 109 and HKT buffer (red line); panels (C) and (D) show the frequency shifts and dissipation
 110 shifts, respectively, corresponding to the 3rd overtone for the adsorption of lipid vesicles
 111 containing variable molar percentages of PtdIns4,5P₂ in HKM buffer. A schematic repre-
 112 sentation of the charge bridging mechanism mediated by Mg²⁺ is shown in panel (E).
 113 The frequency shifts presented in panels (A) and (C) were normalized by the overtone
 114 number. The overtones $n=3,5,7,9$, and 11 are presented in **Figure S1**.

115

116 Since the phosphorylated inositol ring of PtdIns4,5P₂ is able to bind intracellular
 117 divalent cations, the effect of Mg²⁺ on the SLBs formation by vesicles fusion was deter-
 118 mined by comparing the effect of HKT buffer (25 mM HEPES pH 7.2, 125 mM potassium
 119 acetate, 1 mM DTT), and of HKM buffer, which is HKT buffer supplemented with 5 mM

120 magnesium acetate (see **Methods** for further details) (**Figure 1 A, B**). An electrostatic,
121 divalent ion-mediated clustering mechanism for PtdIns4,5P₂ has been demonstrated
122 both by experimental and theoretical (atomistic molecular dynamics simulations) studies
123 of biomimetic model membranes ^{26–28}.

124 Independently of the presence of Mg²⁺, the interaction of the vesicles with the
125 substrate surface yields a decrease of Δf together with the increase of ΔD . This is a clear
126 signature of the adsorption of vesicles on the crystal surface ¹¹. Nevertheless, this inter-
127 action appears to be Mg²⁺-dependent, leading to different profiles for this interaction de-
128 pending on the presence or absence of the divalent cation.

129 In the absence of Mg²⁺, the interaction of the vesicles in HKT with the crystal
130 leads to an initial sharp decrease of $\Delta f/n$, followed by its monotonous increase up to a
131 value of -30 Hz. Similar dependence was found for the ΔD , which evidences an initial
132 sharp increase followed by a monotonous decrease until reaching a constant value over
133 time. These results are compatible with the well-known two-step mechanism of adsorp-
134 tion and fusion of unilamellar lipid vesicles to form SLBs ¹¹. Thus, the process can be
135 interpreted considering an initial adsorption of the vesicles until a critical surface cover-
136 age is reached (characterized by a minimum on Δf and a maximum on ΔD curves in
137 **Figure 1 A, B** and **Figure S1**), followed by vesicle rupture and fusion, giving rise to the
138 formation of planar SLBs (**Figure 1 A, B** and **Figure S1**).

139 On the other hand, in the presence of 5 mM Mg²⁺, the interaction of the vesicles
140 with the silicon dioxide surface is characterized by a monotonous decrease of the Δf and
141 an increase of the ΔD . This is reminiscent from a situation characterized by a faster fu-
142 sion of the vesicles upon their interactions with the surface. These results highlight the
143 role of the divalent cation Mg²⁺ as a fusogenic agent, leading to faster adsorption and
144 fusion kinetics. Similar observations were previously reported for SLBs with different lipid
145 compositions, where the fusogenic effect induced by the divalent cation was proven to
146 be ion-dependent ^{14,15}. The fusogenic character of divalent cations is associated with its

147 role in the mediation of vesicle-substrate interactions by charge bridging (see **Figure 1**
148 **E**). The Mg^{2+} cations are therefore able to mediate charge-bridges between the nega-
149 tively charged PtdIns4,5P₂ lipids and the negatively charged surface of the quartz sen-
150 sor. It should be noted that even though the mechanisms of SLB formation in the pres-
151 ence and absence of Mg^{2+} are intrinsically different, the final values of Δf and ΔD are
152 similar, suggesting that the obtained SLBs present similar structure and mechanical
153 properties independently of the formation pathway. Notably, Luchini et al. studied a sim-
154 ilar system where vesicles comprised by POPC and 1,2-dioleoyl-sn-glycero-3-phospho-
155 (1'-myo-inositol-3',4',5'-trisphosphate), DOPIP₃, were studied by QCM-D and NR ²⁹. The
156 values of Δf obtained are comparable to those reported in this work, however the ΔD
157 values are remarkably smaller than those shown here. This difference is likely related
158 with the inclusion of PE lipids in our system, a kind of phospholipid molecules character-
159 ized by large negative curvatures ³⁰. In fact, a recent work published by Lind et al. demon-
160 strated the formation of POPG-POPE SLBs with full coverage. The QCM-D analysis of
161 this system yielded high ΔD values and spreading of overtones ³¹. These characteristics,
162 also observed in the present study, are hallmarks of non-rigid films and are likely induced
163 by the presence of PE lipids.

164 Although similar studies have been already performed for POPC ¹⁴ and DOPC ¹⁵
165 vesicles, no studies have been reported for DOPC/DOPE lipid mixtures, and vesicles
166 containing PtdIns4,5P₂ lipids. Nevertheless, it is expected that other divalent ions (*e.g.*
167 Ca^{2+} , Sr^{2+}) might induce similar effects, as previously demonstrated in analogous sys-
168 tems ^{14,15}, however such analysis was not carried out as it is outside the scope of this
169 work.

170

171 **Effect of PtdIns4,5P₂ concentration in the fusion process: monotonic vs two step**
172 **fusion**

173

174 The results reported above suggest that the anionic character of PtdIns4,5P₂
175 plays a central role on the Mg²⁺-mediated fusion of lipid vesicles. To obtain a deeper
176 understanding of this, the interaction of vesicles containing DOPC, DOPE and variable
177 molar percentages of PtdIns4,5P₂ (see **Table S1**) with the negatively charged sensor
178 surface was studied by QCM-D experiments. **Figure 1 C, D** show the effect of
179 PtdIns4,5P₂ concentration on the Δf and ΔD during the formation of bilayers as result of
180 the fusion of vesicles containing DOPC, DOPE and variable amounts of PtdIns4,5P₂.
181 Even though the variable composition of the unilamellar lipid vesicles does not have any
182 effect on the ability of the vesicles to form SLBs upon interaction with the negatively
183 charged surface of the sensor, the mechanism of the bilayer formation is dependent on
184 the molar percentage of PtdIns4,5P₂. Thus, while in the case of low PtdIns4,5P₂ content
185 (2% and 4%) a mechanism characterized by a fast adsorption followed by a slow fusion
186 and reorganization of the lipids to form the final SLB is observed, increasing the
187 PtdIns4,5P₂ amount (8% and 10%) leads to a second mechanism characterized by a
188 slower adsorption on the surface, although with a faster fusion of the vesicles, as evi-
189 denced by the monotonous decrease of the Δf (and increase of the ΔD) from the initial
190 stages of the interaction between the vesicles and the solid surface. In fact, this monot-
191 onous change of the Δf and ΔD indicates that vesicles with the highest PtdIns4,5P₂ fuse
192 immediately upon contact with the silicon substrate. This confirms the important role that
193 the anionic phosphorylated inositol headgroup of PtdIns4,5P₂ plays in the interaction with
194 cations, such as Mg²⁺, in the adsorption behavior and fusion kinetics of lipid vesicles.
195 This observation is in agreement with previous studies ³². In fact, strong electrostatic
196 contributions can favor an instantaneous vesicles fusion without requiring a minimal crit-
197 ical coverage of the surface ³³. Furthermore, the PtdIns4,5P₂ content is linked to the final
198 properties of the SLB as highlighted by the increase of the absolute value of the Δf and
199 the ΔD (see **Figure 1 C, D** and **Figure S2**). This may be explained in terms of the charge-
200 bridging contributions, which affect both the kinetics of SLB formation and the

201 homogeneity of the final bilayer structure. High concentrations of PtdIns4,5P₂ induce
202 strong attractive interactions between vesicles and substrate, causing local deformations
203 in the vesicles and reducing their confinement within the bilayer structure, leading to a
204 more uniform homogeneous bilayer. This may be understood considering that for highly
205 charged vesicles it is not required a critical coverage for starting their rupture. Moreover,
206 if the fusion process is slowed down, for example when PtdIns4,5P₂ content is reduced,
207 more heterogenous bilayer are formed, as suggested by the increased spreading of the
208 overtones and higher values of ΔD (**Figure S2**). The smaller deformation of the vesicles
209 upon contact with the surface results in reduced local instabilities of the lipid vesicles,
210 minimizing the instantaneous rupture events of the liposome when in contact with the
211 substrate surface ¹³, resulting probably in the formation of bilayers with an asymmetric
212 in-plane lateral packing and perpendicular distribution of the lipids between both leaflets,
213 reducing the compactness of the obtained bilayers ³³. This hypothesis agrees with the
214 changes reported in the QCM-D parameters *i.e.* higher absolute values of Δf and ΔD
215 observed as the PtdIns4,5P₂ concentration decreases (**Figure 1 C, D** and **Figure S2**).
216 The former parameter (Δf) is related to the formation of thicker films, whereas the in-
217 crease of the ΔD is indicative of the heterogeneity of the films. Indeed, the in-plane and
218 perpendicular heterogeneities of the formed bilayers are expected to oscillate with an
219 associated delay compared to the homogenous bilayers. Thus, a non-rigid behaviour is
220 expected, which is characterized by increased values of ΔD and spreading of the over-
221 tones, as observed in **Figure 1 C, D** and **Figure S2**.

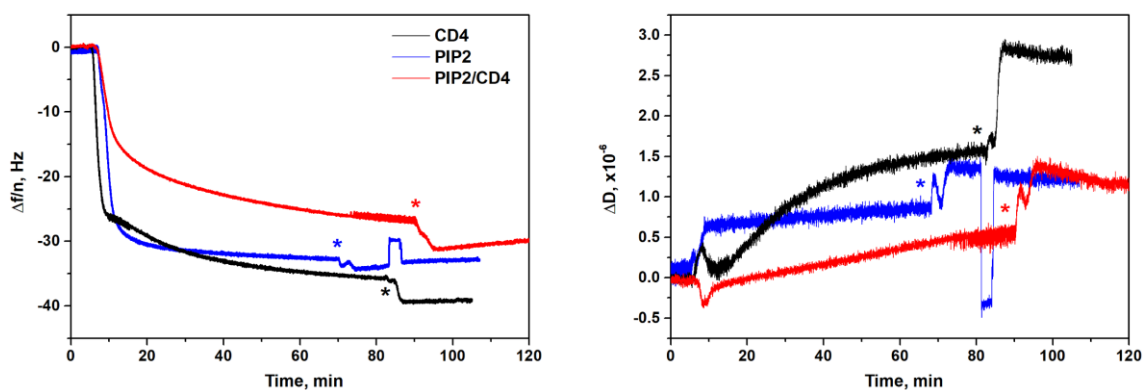
222

223 **SLBs with lipid/peptide conjugates as mimics of protein membrane receptors:**

224 **deposition and structure by QCM-D**

225 The main goal of this work is to design SLBs incorporating peptides mimicking
226 the cytoplasmic ligands from transmembrane proteins. To this end, CD4 lipid-peptide
227 conjugate was included within the lipid mixture used for the preparation of unilamellar

228 vesicles and studied by QCM-D (see **Table S1** for compositions and **Methods** for vesicle
229 preparation). **Figure 2** displays the time dependence of the Δf and ΔD for the adsorption,
230 and subsequent fusion of vesicles including CD4 lipid-peptide conjugate in the presence
231 and absence of PtdIns4,5P₂, as obtained in the HKM buffer.



232

233 **Figure 2:** Vesicle adsorption and fusion kinetics: frequency shift (A) and dissipation shift
234 (B) plots corresponding to the 3rd overtone for unilamellar lipid vesicles composed of
235 DOPC, DOPE and the CD4 lipid-conjugate in presence and absence of PtdIns4,5P₂.
236 Experiments were performed in HKM buffer. The frequency shifts presented in panel (A)
237 were normalized by the overtone number. * highlights the start of washing step.

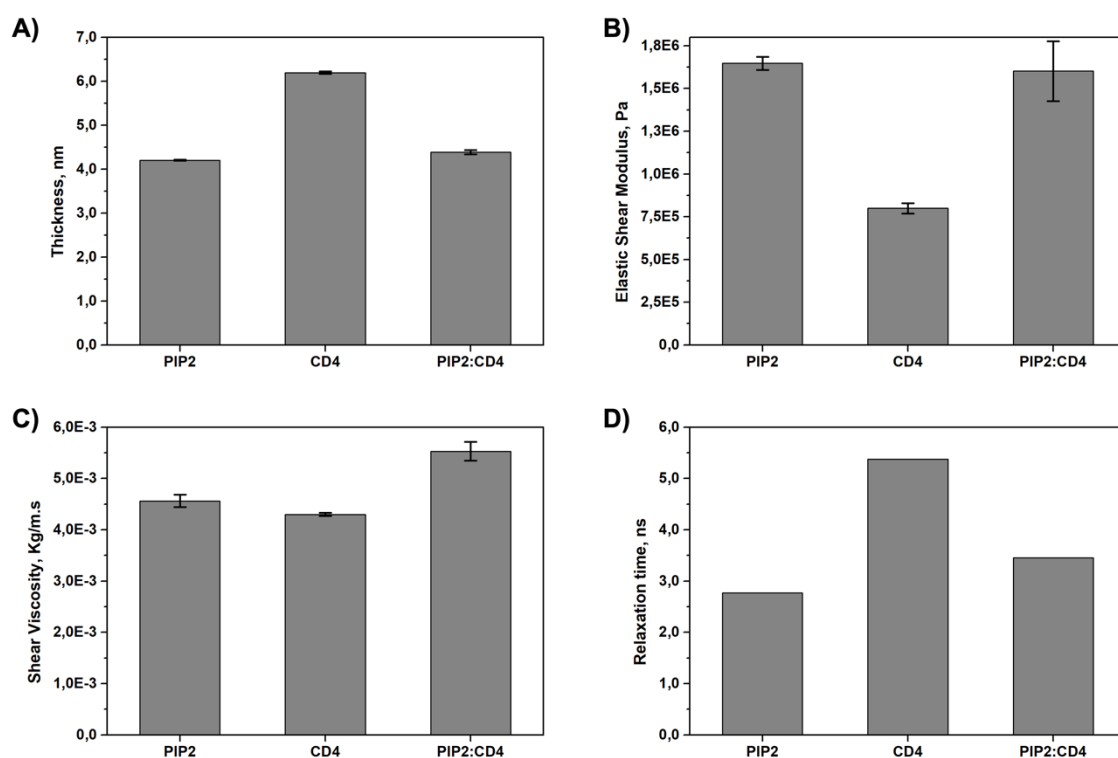
238

239 The presence of PtdIns4,5P₂ emerges as a very important contribution to the final
240 characteristic of the obtained SLBs. In fact, the magnitude of the Δf and ΔD are smaller
241 in the presence of PtdIns4,5P₂ for the liposomes containing the CD4 lipid-peptide conju-
242 gate. This may be interpreted by considering that the electrostatic contributions associ-
243 ated with presence of PtdIns4,5P₂ favours the fusion of the unilamellar vesicles due to
244 the interaction with Mg²⁺, thus leading to the formation of a more homogeneous SLB.
245 This is supported by smaller values of Δf , which is also an indication of a smaller average
246 thickness of the SLB, associated with a reduced probability of the imbibition of intact
247 vesicles with the lipid bilayer. In addition, the time evolutions of the ΔD and overtone
248 spreading also confirm the higher heterogeneity of the bilayers obtained in the absence
249 of PtdIns4,5P₂ (**Figure 2** and **Figure S3**). The non-monotonous change of the ΔD with
250 time in absence of PtdIns4,5P₂ suggests a more complex mechanism of SLB formation.
251 This description agrees with the evolution of the ΔD versus $\Delta f/n$ plots displayed in **Figure**
252 **S4** for the formation of different composition SLBs. Thus, while for SLBs with PtdIns4,5P₂

253 in the absence and presence of CD4, the ΔD increases quasi-monotonously as the ad-
254 sorption proceeds (defined in terms of the decrease of the Δf), in the absence of
255 PtdIns4,5P₂, the evolution of the corresponding ΔD versus $\Delta f/n$ plot (see **Figure S1**) is
256 not monotonous, suggesting a possible initial adsorption of intact vesicles on which the
257 latter are fused as indicated by the presence of a minimum in the curve. Based on our
258 results, it is therefore clear that PtdIns4,5P₂ plays an important role on the formation of
259 SLBs.

260 After being deposited, the structure and mechanical properties of the SLBs de-
261 posited on the surface of the quartz sensor were calculated by the Voigt-Voinova visco-
262 elastic model³⁴ (see **Methods** for further details). This is necessary because the Sauer-
263 brey equation that linearly relates Δf with material deposited onto the crystal is no longer
264 valid for the studied bilayers due to their non-rigid character³⁵⁻³⁷. Therefore, the validity
265 of the Voinova-Voigt for describing the behavior of the obtained bilayers is supported in
266 two conditions: (i) the non-rigid character of lipid bilayers, evidenced by the spread of the
267 frequency shifts corresponding to the different measured overtones and the relatively
268 high changes of the dissipation factor, which is mostly due to the distribution of the water
269 molecules surrounding the polar head-groups (confirmed by **NR**, see next section), re-
270 sults in frictional (viscous) contributions and crystal oscillation dampening, and (ii) the
271 spatial arrangement of the lipid bilayers observed by AFM images (**Figure 4**) which con-
272 firms the homogenous 3D organization of the bilayers, allowing us to consider them as
273 a single layer undergoing a delayed displacement in relation to the quartz crystal³⁸.

274 To summarize, the thickness and mechanical properties of SLBs with the previ-
275 ous mentioned compositions (DOPC:DOPE:PtdIns4,5P₂, DOPC:DOPE:CD4 and
276 DOPC:DOPE:PtdIns4,5P₂:CD4), calculated through the Voigt-Voinova model, are re-
277 ported in **Figure 3**. The resulting bilayer thickness was plotted in panel **A**, elastic shear
278 modulus (μ_f) in **B**, shear viscosity (η_f) in **C**, and relaxation time ($\tau_f = \eta_f / \mu_f$) in **D**, which
279 provides a ratio between the different contributions to the viscoelastic response.



281

282 **Figure 3:** Properties of SLBs obtained from QCM-D analysis. The parameters were ex-
 283 tracted by using the Voigt-Voinova viscoelastic model. (A) Thickness. (B) Elastic shear
 284 modulus. (C) Shear viscosity. (D) Relaxation time.

285

286 As expected, differences in the parameters are observed depending on the spe-
 287 cific lipid compositions. In the case of SLBs composed of DOPC, DOPE and PtdIns4,5P₂
 288 with or without CD4, the thickness in the order of 40 - 60 Å is similar to a typical DOPC
 289 bilayer (see **Figure 3A**)³⁹⁻⁴³. However, in absence of PtdIns4,5P₂, there is a ~1.5 fold
 290 increase in thickness for a SLB containing CD4, thereby suggesting the peptide pro-
 291 trudes from the SLB. Furthermore, the peptide embedded in the lower leaflet of the SLB
 292 increase the spacing between the sensor surface and the bilayer. Surprisingly, when
 293 PtdIns4,5P₂ is combined with CD4 in the SLB, a different scenario is observed. Although
 294 it was expected that the presence of CD4 lipid-peptide conjugate within the SLB would
 295 increase the average SLB thickness in comparison to a bilayer composed solely of lipids,
 296 this behavior was only observed when the CD4 was embedded in the PM in the absence
 297 of PtdIns4,5P₂. Curiously, the simultaneous insertion of CD4 lipid-peptide conjugate and

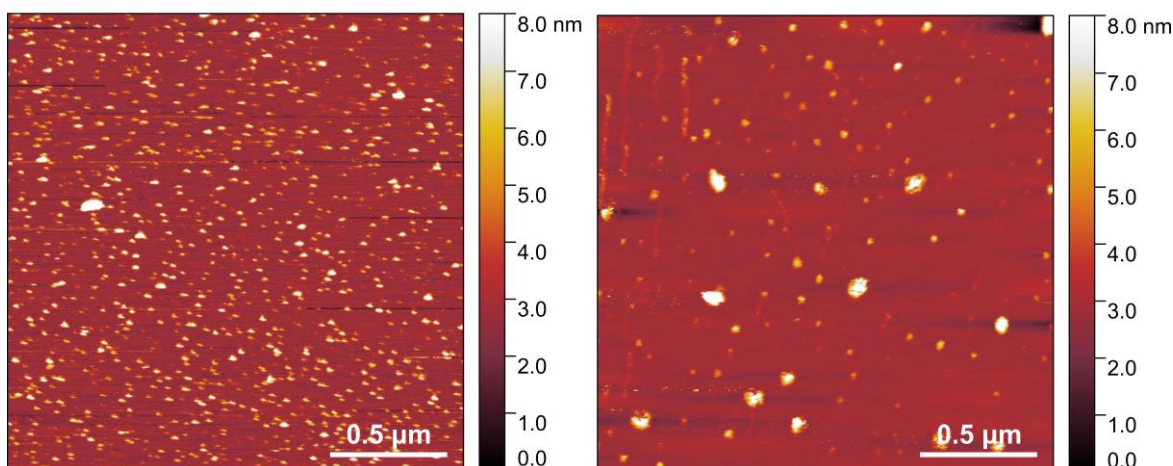
298 PtdIns4,5P₂ in the SLB resulted in a reduction of the average thickness of the film. This
299 effect can be explained considering the electrostatic attraction between the CD4 poly-
300 peptide chain, hypothesized as a random coil chain bearing a total net positive charge,
301 and the negatively charged headgroup of PtdIns4,5P₂. As a result of this electrostatic
302 interaction CD4 is placed at the level of the lipid headgroups, as demonstrated by NR in
303 the next section, and, as a consequence, preventing its polypeptide chains to protrude
304 towards the bulk phase (See scheme in **Figure 5G**). Besides, AFM images reported in
305 **Figure 4** also shown how the electrostatic interaction of CD4 with PtdIns4,5P₂ gives rise
306 to a reduction in the lipid phase demixing by decreasing the number of PtdIns4,5P₂ clus-
307 ters.

308 Similarly, to the variability in the thickness of the SLBs, the mechanical properties
309 were also found to be dependent on the lipid composition and the presence of CD4. In
310 the absence of CD4, the values of shear elasticity modulus and viscosity are in good
311 agreement with previous reports for SLBs composed of POPC³⁸. The incorporation of
312 CD4 into the bilayers increases the shear viscosity and, therefore, the viscoelastic relax-
313 ation time in a manner strongly dependent on SLB specific composition. In the presence
314 of CD4 and no PtdIns4,5P₂, the relaxation time is ~1.5-folds higher than that correspond-
315 ing to bilayers with both PtdIns4,5P₂ and CD4, and ~2-folds higher than that of bilayers
316 with PtdIns4,5P₂ and without CD4. This reflects the higher resistance to motion in the
317 former SLB due to the bilayer strong heterogeneity character.

318

A) DOPC:DOPE:PtdIns4,5P₂

B) DOPC:DOPE:PtdIns4,5P₂



319

320 **Figure 4:** Membrane phase demixing and PtdIns4,5P₂ clusterization is also dependent
321 on the presence of CD4. SLBs composed by DOPC:DOPE:PtdIns4,5P₂ (A) and
322 DOPC:DOPE:PtdIns4,5P₂:CD4 (B) in HKM buffer are examined by fluid-phase peak
323 force tapping mode AFM. Scale bars are 0.5 μm.

324

325 **Further determination of the SLBs structure by Neutron Reflectometry**

326

327 NR elucidates the structure and composition of SLBs in the direction perpendic-
328 ular to the plane of the membrane with sub-nanometric resolution. A 1D profile of the
329 reflectivity (R), defined as the ratio of neutrons reflected from the interface over the inci-
330 dent intensity of the neutron beam, is measured in specular conditions as a function of
331 the momentum transfer vector normal to the interface, $Q_z = 4\pi \sin \theta / \lambda$, where θ is the
332 angle of incidence and λ is the wavelength of the neutron beam.

333 Here, SLBs composed of DOPC:DOPE:PtdIns4,5P₂ and also enriched in CD4
334 dileucine motifs were found to be laterally homogeneous on the length scale of the in-
335 plane neutron coherence length, on the order of several microns⁴⁴. This implies that the
336 measured R(Q_z) profile can be linked with an in-plane averaged scattering length density
337 (SLD) depth profile across the membrane delimited by this coherence length and, there-
338 fore, the structure of the membrane can be determined as a function of the distance from
339 the silicon substrate surface. The goal was to elucidate the structural differences of the

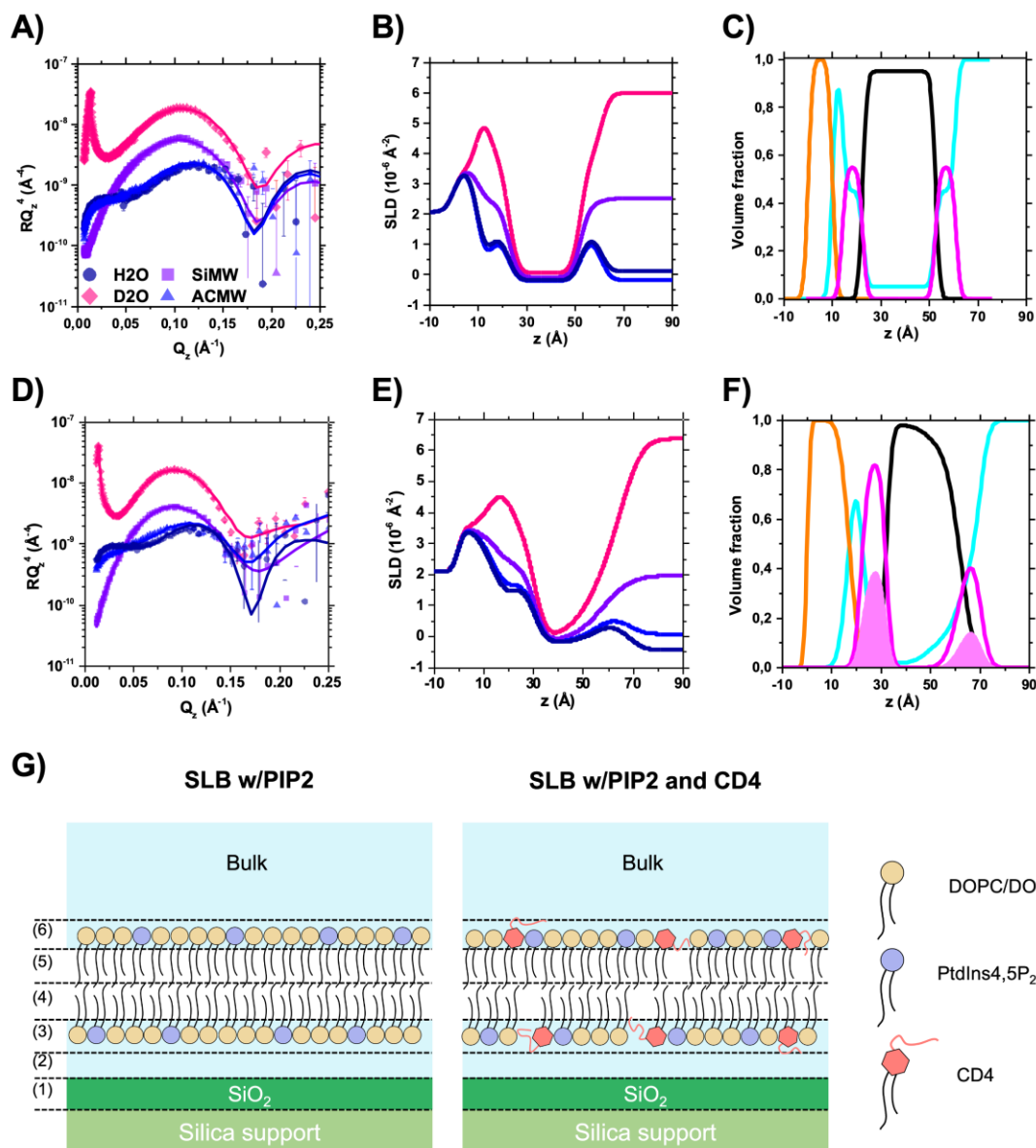
340 SLBs due to the presence of the CD4 short, random coil peptide. By simultaneously
341 fitting NR profiles measured in 4 isotopic contrasts, the position of the CD4 peptide was
342 determined in the direction perpendicular to the plane of the membrane with emphasis
343 on the evaluation and molar quantification of CD4 peptide asymmetric distribution in be-
344 tween leaflets. The isotopic contrasts used in the experiments consisted of HEPES-NaCl
345 buffer prepared in (1) pure D₂O, (2) pure H₂O, (3) silicon-matched water (SiMW), which
346 is a mixture of D₂O:H₂O that contrast match the SLD of the silicon crystal ($2.07 \cdot 10^{-6} \text{ \AA}^{-2}$),
347 and (4) air contrast-matched water (ACMW), which is characterized by an SLD=0.

348 NR data of PtdIns4,5P₂ containing SLBs, in the absence of CD4, were fitted with
349 a model (illustrated in **Figure 5G**) consisting of 5 layers defining the lipid bilayer, includ-
350 ing both inner and outer leaflets, a wetting layer of water between the inner lipid leaflet
351 and the native SiO₂ layer, that naturally grows on silicon substrates whose thickness was
352 determined prior to the bilayer deposition (see **Table S3**). Each layer was characterized
353 by a thickness, an interfacial roughness, an in-plane average SLD and an averaged mo-
354 lecular volume of the molecular components (see **Tables S2 and S3 and Figure 5G** for
355 a scheme of the model). The NR profiles were fitted in each contrast buffer as shown by
356 the good agreement between the fitting curves and the experimental reflectivity data
357 plotted as RQ_z^4 vs Q_z (to emphasize the fine details of the modeling at high Q_z values)
358 in **Figure 5 A**. The bilayer was modelled considering two layers for inner and outer lipid
359 headgroups and one intermediate layer defining the aliphatic tails region (layers 4 and
360 5, **Figure 4 SLB w/PIP2**, are considered as one layer), which is formed by two identical
361 lipid leaflet acyl tails, yielding a thickness of 30 Å and a water content of 4%, thus con-
362 firming high lipid coverage. Moreover, a water layer of 4 Å between the bilayer and the
363 silicon crystal was also considered. The resulting SLD profiles for each contrast are re-
364 ported in **Figure 5 B**. From the SLD distribution as a function of the distance to the silicon
365 substrate, the variation of the volume fraction profiles of each layer was calculated using
366 the difference of two error functions (see **Methods**) and plotted in **Figure 5 C**. The area-
367 per-molecule (APM) obtained was $\sim 70 \text{ \AA}^2$ and the total thickness was found to be 46 Å

368 in agreement with QCM data (see **Figure 3 A**) and similar systems studied in the litera-
369 ture ^{29,45}.

370 In the presence of CD4 (NR profiles shown in **Figure 5 D**), the bilayer resulted in
371 an asymmetrical structure composed by two lipid leaflet acyl tails with different thickness:
372 13 Å the outer, in contact with the bulk phase and 17 Å the corresponding to the inner
373 leaflet in contact with the solid support. The total size of the bilayer, calculated through
374 a 6-layer model, resulted in 48 Å, again in agreement with QCM data (see **Figure 3 A**).
375 An increase of the thickness of the inner headgroup was observed with respect to the
376 sample in absence of CD4, together with a decrease of the water content (see **Figure 5**
377 **C, F**). The higher percentage of CD4 conjugate in the inner leaflet increase both tails and
378 headgroups layer thickness. Regarding the headgroups, this is due to the presence of
379 the peptide, which also reduces the water volume fraction. In addition, although the lipid
380 conjugated to CD4 (**Figure S3**) contains 16-carbon atoms acyl chains, against the 18-
381 carbon atoms chains of DOPC and DOPE lipids, its presence increases the orientation
382 order of the hydrocarbon tails giving rise to a remarkable increase in the thickness. These
383 facts together make an asymmetric APM distribution per leaflet (see **Table S2**). Finally,
384 as already obtained from the analysis of QCM-D experimental data, the values of thick-
385 ness for the two PtdIns4,5P₂-containing bilayers, with and without CD4, are similar, thus
386 confirming that the random coil peptide prefers laying on the bilayer, rather than extend-
387 ing away from it, being attracted by the PtdIns4,5P₂ negative charges. The formation of
388 enriched PtdIns4,5P₂ SLBs with an asymmetric, quantifiable presence of lipo-peptides
389 containing the dileucine motif from the T-cell surface antigen protein CD4, can open an
390 avenue to the rational design of complex peptide/lipid biomimetic membranes analysed
391 not only by QCM-D and NR but also by other surface sensitive techniques ^{9,46} and solid-
392 state NMR ^{47,48}, therefore providing complementary information for a broader under-
393 standing of these type of systems.

394



395

396 **Figure 5:** Reflectivity profiles of (A) DOPC:DOPE:PtInS4,5P₂ (70:20:10) and (D)
 397 DOPC:DOPE:PtInS4,5P₂:CD4 (66.5:20:10:3.5) in the 4 contrasts: H₂O (dark blue circle), ACMW (blue triangles), SiMW (violet squares) and D₂O (pink diamonds). The relative fits are presented as lines. (B) and (E) show the SLD profiles perpendicular to the interface of DOPC:DOPE:PtInS4,5P₂ (70:20:10) and DOPC:DOPE:PtInS4,5P₂:CD4 (66.5:20:10:3.5) respectively: H₂O (dark blue line), ACMW (blue line), SiMW (violet line) and D₂O (pink line). (C) and (F) report the volume fraction profiles perpendicular to the interface, showing the contribution of silicon oxide (orange line), aliphatic tails (black line), hydrophilic headgroups (magenta), and water (cyan line). The volume fraction related to CD4 peptide moiety is shown as light pink area in (F). (G) Schematic representation of the SLB surface after incorporation of PtInS4,5P₂ lipids (shown as purple circles) and in the presence and absence of the lipid-peptide conjugate CD4 (shown as salmon hexagon). The NR fitted parameters for the layers 1 to 6 can be found in **Table S2**.

410

411

412 **Conclusion**

413 An *in vitro* model based on SLBs composed of DOPC:DOPE:PtdIns4,5P₂ and en-
414 riched in CD4 dileucine lipo-peptide conjugates was studied by a combination of NR,
415 AFM and QCM-D techniques. The effect of Mg²⁺ on SLB formation indicates that divalent
416 cations can mediate the interaction between the negatively charged PtdIns4,5P₂-con-
417 taining liposomes and QCM-D sensor surface promoting a faster adsorption and fusion
418 kinetics. In addition, increasing amounts of PtdIns4,5P₂ were screened to determine how
419 its anionic character influences vesicle adsorption, fusion kinetics and SLBs formation.
420 Higher levels of PtdIns4,5P₂ in the SLBs were crucial for the creation of homogenous
421 SLBs. These also affected the mechanism of formation showing a transition from a single
422 to a two-step process in the time scale of the QCM-D experiments. Overall, this multi-
423 technique approach combining NR, AFM and QCM-D provided results regarding the me-
424 chanical properties as well as out-of-plane structure of the SLBs in the presence and
425 absence of lipo-peptide conjugate CD4.

426 In conclusion, this work will contribute towards a better design of *in vitro* model sys-
427 tems based on SLBs that incorporate peptides as mimics of protein ligands. The inter-
428 action between PtdIns4,5P₂ and CD4 lipo-peptides might have a direct influence on
429 membrane curvature, modulating the binding of different peripheral membrane proteins
430 which are fundamental events in the initiation of the CME pathway.

431

432 **Materials and Methods**

433

434 **Materials**

435 The lipids (see **Figure S5**), 1,2-dioleoyl-sn-glycero-3-phosphocholine (DOPC, ≥
436 99,0% purity), 1,2-dioleoyl-sn-glycero-3-phosphoethanolamine (DOPE, ≥ 99,0% purity)
437 and L-α-phosphatidylinositol-4,5-bisphosphate (ammonium salt) (PtdIns4,5P₂, ≥ 99,0%
438 purity) were supplied by Avanti Polar Lipids Inc. (Alabaster, USA) and used without

439 further purification. CD4 peptide was covalently linked to the synthetic lipid 16:0 MPB
440 PE, 1,2-Dipalmitoyl-sn-Glycero-3-Phosphoethanolamine-N-[4-(p-maleimidophenyl) bu-
441 tyramide]. A detailed description of the synthesis process of the lipid-peptide conjugates
442 can be found in the work by Höning et al. ⁶.

443 The experiments were performed in HKM buffer pH = 7.2, whose composition is
444 the following: 25 mM HEPES (4-(2-hydroxyethyl)piperazine-1-ethanesulfonic acid and
445 N-(2-hydroxyethyl)piperazine-N'-(2-ethanesulfonic acid)), 125 mM potassium acetate, 5
446 mM magnesium acetate, and 1 mM DTT (threo-1,4-dimercapto-2,3-butanediol). HEPES
447 (in solution (1 M in H₂O) and powder (≥ 99.5% purity)), potassium acetate (≥ 99,0% pu-
448 rity), magnesium acetate (≥ 99,0% purity), and DTT (≥ 99,0% purity) were purchased
449 from Sigma Aldrich (Saint Louis, MO, USA). An analogous version of this buffer, named
450 HKT buffer, was prepared following the same composition without adding magnesium
451 acetate.

452 The phospholipid solutions were prepared by dissolving the lipid powder (DOPC,
453 DOPE and PtdIns4,5P₂) in chloroform until a final concentration of 1.0 mg·mL⁻¹. All the
454 solutions were then stored on the freezer, at a temperature below -20 °C, until further
455 use. Ultra-pure water was generated by passing deionized water through a Milli-Q unit
456 (total organic content=4 ppb; resistivity=18 MΩ·cm, Milli-Q, Merck KGaA, Darmstadt,
457 Germany).

458

459 **Vesicle preparation**

460

461 The phospholipid and CD4 solutions, previously dissolved in chloroform, were mixed
462 according to the desired composition, inside glass vials. The molecular ratios used for
463 the different components are shown in **Table S1**. The volatile solvent was evaporated
464 under a continuous stream of argon, and then the glass vials were left under vacuum
465 overnight to ensure evaporation of any remaining solvent.

466 In order to obtain samples suitable for QCM-D measurements, the resulting lipid
467 films (sample from #1 to #4, **Table S1**) were re-hydrated with a mixture of buffer:water
468 (in volume ratio of 8:2, respectively) up to a final lipid concentration of 0.1 mg·mL⁻¹. The
469 samples were left overnight at room temperature with end-over-end rotation. The mul-
470 tilamellar vesicles formed after hydration were then subjected to a series of treatments
471 (freeze-thaw, tip sonication and extrusion) to convert them into unilamellar vesicles (**Fig-**
472 **ure S6** and **Table S4**). First, the vesicles were subjected to 5-10 successive freeze-thaw
473 cycles with liquid nitrogen and ice, then tip sonicated (Sonopuls HD 2200, Bandelin, Ger-
474 many), with a titanium probe (MS73 with microtip of 3 mm), for 15-20 min, with repeated
475 on/off pulses of 2 s and 3 s, respectively, and power amplitude of 20%. Finally, the ves-
476 icle dispersions were manually extruded using a commercial mini extruder kit (Avanti
477 Polar Lipids, AL, Alabaster, USA) assembled with polycarbonate membranes (Whatman
478 Inc., Clifton, NJ, USA) of 100 nm pore size. The extrusion cycles were repeated 15-25
479 times and the obtained dispersions of vesicles were stored at 4 °C until experiment. The
480 size of the unilamellar lipid vesicles was monitored through dynamic light scattering
481 (Zetasizer Nano ZS90, Malvern Instruments, U.K.), before injection into the QCM-D. The
482 measurements were performed with temperature-control set at 20 °C and the scattering
483 angle at 90°, showing the formation of lipid vesicles with monodisperse size distributions
484 and diameter close to 100 nm (**Table S5**).

485 To produce SLBs for NR experiments, the lipid films (samples #2 and #4, **Table S1**)
486 were re-hydrated at room temperature in HEPES 5 mM, NaCl 150 mM, MgCl₂ 3 mM
487 buffer, up to 1 mg·mL⁻¹ lipid concentration, and vortexed to fully suspend vesicles. Im-
488 mediately before use, the suspensions were tip sonicated for 5 min at pulses of 1 s on/off.
489

490 **QCM-D Measurements**

491

492 QCM-D experiments were performed using a commercial Q-Sense E4 instrument
493 (Q-Sense, Biolin Scientific AB, Göteborg, Sweden) fitted with SiO₂-coated AT-cut quartz

494 sensors (Q-Sense, Biolin Scientific AB, Göteborg, Sweden). These sensors
495 were thoroughly cleaned, prior to their use, in an ultrasound bath by sequential immer-
496 sion in chloroform, acetone, ethanol and water. Afterwards, the cleaned sensors were
497 dried under a gentle stream of nitrogen and exposed to UV-ozone cleaning in a Pro-
498 Cleaner™ Plus instrument (BioForce Nanosciences, Virginia Beach, VI, USA) for 30
499 minutes. The crystals were then immersed in water and dried under a gentle stream of
500 nitrogen. The cleaned and hydrophilized crystals were immediately fitted inside the
501 QCM-D flow module. The flow module was then connected to a peristaltic pump (Multi-
502 channel Peristaltic Pump IPC-N 4, Ismatec, Switzerland) operating with a fixed flow rate
503 of 0.10 mL·min⁻¹.

504 QCM-D measures the impedance spectra of the quartz crystal for the fundamen-
505 tal frequency ($f = 5$ MHz) and odd overtones up to the 13th. Before the experiments, the
506 fundamental frequencies of the overtones were recorded up to the equilibration of the
507 signal at the experimental temperature (20 °C), which is evidenced for a stable baseline,
508 *i.e.*, the Δf and ΔD remaining constant for at least 5 minutes. After equilibration in buffer,
509 the lipid vesicles dispersion (0.10 mg·mL⁻¹) is introduced in the flow cell and left under
510 incubation for 20-40 minutes, allowing the adsorption and fusion processes. The meas-
511 urements were performed using freshly prepared vesicles that were stored at a temper-
512 ature of 4°C for a maximum of ~ 12 hours (overnight).

513 The QCM-D allows monitoring, simultaneously, the changes of the Δf and ΔD
514 over time. The QCM-D data were analysed using the software Q-Tools (version 3.0.10,
515 Q-Sense, Biolin Scientific AB, Göteborg, Sweden), which is based in the model proposed
516 by Voinova et al. ³⁴. This procedure makes it possible to correlate the changes in the
517 resonant frequency and dissipation factor of the different overtones with physical param-
518 eters of the layers (thickness t_j , density ρ_j , elasticity μ_j and viscosity η_j), according to the
519 following two equations (Note: *The fundamental frequency is not used for data analysis*
520 *due to the noisy character of its signal*):

521
$$\Delta f \approx -\frac{1}{2\pi\rho_q t_q} \left\{ \frac{\eta_l}{\delta_l} + \sum_{f=1,2} \left[t_f \rho_f \omega - 2t_f \left(\frac{\eta_l}{\delta_l} \right)^2 \frac{\eta_f \omega^2}{\mu_f^2 + \omega^2 \eta_f^2} \right] \right\}$$
 6)

522
$$\Delta D \approx \frac{1}{2\pi f \rho_q t_q} \left\{ \frac{\eta_l}{\delta_l} + \sum_{f=1,2} \left[2t_f \left(\frac{\eta_l}{\delta_l} \right)^2 \frac{\mu_f \omega}{\mu_f^2 + \omega^2 \eta_f^2} \right] \right\}$$
 (7)

523 where ρ_q and t_q are the density and thickness of the quartz crystal sensor, η_l and δ_l
 524 are the density of the liquid and viscous penetration depth of the shear wave in the bulk
 525 liquid, ω is the angular frequency of the oscillation^{34,49,50}. For the fitting of experimental
 526 data, the fluid density and viscosity were fixed at $1.0 \times 10^3 \text{ kg}\cdot\text{m}^{-3}$ and $1.0 \times 10^{-3} \text{ kg}\cdot\text{m}^{-1}\cdot\text{s}^{-1}$,
 527 respectively, as all experiments were conducted in aqueous dispersions. The density of
 528 the lipid bilayer was fixed at $1.1 \times 10^3 \text{ kg}\cdot\text{m}^{-3}$, which is consistent with previous studies¹¹.

529

530 **Neutron Reflectometry Data Acquisition**

531

532 Neutron Reflectometry experiments were performed on the time-of-flight horizontal
 533 reflectometer FIGARO at the Institut Laue-Langevin (ILL), Grenoble (France)⁵¹. Two
 534 different angles of incidence ($\theta = 0.8^\circ$ and 3.2°) and a wavelength resolution of 7% $d\lambda/\lambda$
 535 were used, yielding a momentum transfer of $7 \times 10^{-3} \text{ \AA}^{-1} < Q_z < 0.26 \text{ \AA}^{-1}$, normal to the
 536 interface.

537 The data were reduced and normalized to a measurement of pure D₂O using COS-
 538 MOS⁵². Custom-made solid/liquid flow cells with polished silicon crystals (111) with a
 539 surface area of $5 \times 8 \text{ cm}^2$ were used. Neutron cell flow modules and O-rings were cleaned
 540 by bath sonication in a Decon90 solution, then in pure water and finally in ethanol. The
 541 crystals were cleaned by bath sonication in chloroform, acetone, ethanol and water. Fi-
 542 nally, the crystals were dried with nitrogen flux and treated with Plasma cleaner for 2 min
 543 before neutron cell assembly. During the measurements, the temperature was main-
 544 tained constant by circulating water from a thermostatic water bath. Variation of the aque-
 545 ous solvent contrast was achieved by exchanging the bulk solvent using a HPLC pump
 546 set to a flow rate of $2 \text{ mL}\cdot\text{min}^{-1}$. After characterization of bare silicon substrate, the

547 dispersion of lipid vesicles was injected by a syringe and incubate for 10 minutes, fol-
 548 lowed by a washing step with pure water to allow SLB formation. The SLB was charac-
 549 terized in 4 different isotopic solvent contrasts: H₂O (SLD = -0.56·10⁻⁶ Å⁻²), ACMW
 550 (91.9:8.1 v/v% H₂O:D₂O, SLD = 0), Silicon matched water (SiMW, 62:38 v/v% H₂O:D₂O,
 551 SLD = 2.07·10⁻⁶ Å⁻²) and D₂O (SLD = 6.36·10⁻⁶ Å⁻²). Each of the above-mentioned con-
 552 trasts includes HEPES 5 mM, NaCl 150 mM buffer (without MgCl₂).

553

554 Neutron Reflectometry Data Modeling

555

556 Modelling of the NR data has been done by approximating the continuous bilayer
 557 structure perpendicular to the plane of the membrane using a model composed of N
 558 layers of varying scattering length density (SLD) and thickness (t) modulated by a rough-
 559 ness (σ) parameter, which describes the interfacial mixing of the layers, as follows:

$$560 \quad \text{SLD}(z) = \sum_{i=0}^N \frac{\text{SLD}_i - \text{SLD}_{i-1}}{2} \left(1 + \text{erf} \left(\frac{z - t_i}{\sigma_i \sqrt{2}} \right) \right) \quad 8)$$

561 The data analysis was performed using MOTOFIT software⁵³. For PtdIns4,5P₂-con-
 562 taining bilayer (no CD4), a symmetric bilayer model was used, that is a 5-layer model,
 563 characterized by two polar headgroups-layers and a unique hydrophobic tails-layer,
 564 which includes the tails from both lipid leaflets, a water layer between bilayer and crystal,
 565 and a Silicon oxide layer (SLD = 3.47 10⁻⁶ Å⁻²). For PtdIns4,5P₂-CD4-containing bilayer,
 566 an asymmetric model was used, in which each tail leaflet was described by a layer, lead-
 567 ing to a 6-layer model. Indeed, the lipid composition in the two leaflets was found to be
 568 different, being the inner leaflet (*i.e.*, the one closer to the silicon substrate) richer in
 569 peptide than the outer one. The fixed parameters used in the fitting procedure (see **Table**
 570 **S2**) are the scattering length densities of heads (SLD_{heads}) and tails (SLD_{tails}), as well as
 571 the molecular volumes (V_{heads} and V_{tails}). Besides, the exchange of labile protons was
 572 considered for the calculation of SLD_{heads}. The thickness of tails (t_{tails}) and headgroups
 573 (t_{heads}) layer, as well as their water content (f_{tails} and f_{heads}), were considered as fitting

574 parameters (see **Table S3**), together with the roughness of each layer. The water volume
575 fraction in the headgroups-layers was constrained to ensure same area-per-molecule
576 (APM) of lipid headgroups and tails, in each layer, $APM = V_i/t_i f_i$ (with i=aliphatic tails or
577 headgroups). Experimental data of SLB in the four solvent contrasts were fitted together.
578 Thus, the ambiguity in the interpretation of the sample structure, which may arise from
579 the different sensitivity that the curves exhibit with respect to the different sample com-
580 ponents, is significantly reduced.

581

582 **Atomic force microscopy**

583

584 Supported lipid bilayers were formed were formed on freshly cleaved mica sur-
585 face (discs with 12 mm diameter). 50 μ L of 1 mg/ml vesicle solution were added on the
586 mica and the sample was placed in a closed petri dish and left to incubate for 30 minutes
587 at room temperature. Later, the sample was washed 4 times with water to remove un-
588 fused vesicles and the SLBs formed were imaged in the presence of buffer in the AFM
589 liquid cell. All images were obtained with a multimode AFM and a Nanoscope V controller
590 (Bruker). The AFM was operated in Peak Force mode in liquid, at room temperature. The
591 Silicon tip on Silicon Nitride Cantilever (Model: PFQNE-AL), with a spring constant 0.8
592 N/m and a resonant frequency 300 kHz, were used for scanning. The images were taken
593 at a scan rate of 1 Hz and 512 x 512 pixels. The images were acquired with the Nano-
594 scope Software. They were topologically flattened and analyzed by using NanoScope
595 Analysis 1.90 software (Bruker) and Gwyddion software (version 2.60).

596

597 **Acknowledgments**

598 The authors thank the Institut Laue-Langevin for the allocation of beamtime and the
599 Partnership for Soft Condensed Matter (PSCM) for the lab support. E.G. and A.M.
600 acknowledge the financial support from MICINN under grants PID2019-106557GB-C21

601 and PID2021-129054NA-I00, respectively. A.M. also acknowledges the financial support
602 received from the IKUR Strategy under the collaboration agreement between Ikerbasque
603 Foundation and Materials Physics Center on behalf of the Department of Education of
604 the Basque Government. I.M.-M. acknowledges the EMBO organization for the EMBO
605 Short-Term Fellowship 8740. D.J.O and N.Z acknowledge financial support from the
606 Wellcome Trust (grant 207455/Z/17/Z) awarded to D.J.O. This work was developed
607 within the scope of the project CICECO-Aveiro Institute of Materials, UIDB/50011/2020
608 and UIDP/50011/2020, financed by national funds through the Portuguese Foundation
609 for Science and Technology/MCTES.

610

611 **Conflicts of Interest**

612 The authors declare no conflict of interest. The funders had no role in the design of the
613 study; in the collection, analyses, or interpretation of data; in the writing of the manu-
614 script, or in the decision to publish the results.

615

616

617 **References**

- 618 1. Di Paolo, G. & De Camilli, P. Phosphoinositides in cell regulation and membrane
619 dynamics. *Nature* **443**, 651–657 (2006).
- 620 2. Phan, T. K. *et al.* Phosphoinositides: multipurpose cellular lipids with emerging
621 roles in cell death. *Cell Death Differ.* **26**, 781–793 (2019).
- 622 3. Hammond, G. R. V *et al.* PI4P and PI(4,5)P2 Are Essential But Independent
623 Lipid Determinants of Membrane Identity. *Science (80-.).* **337**, 727–730 (2012).
- 624 4. Martin, T. F. J. PI(4,5)P2 regulation of surface membrane traffic. *Curr. Opin. Cell*
625 *Biol.* **13**, 493–499 (2001).
- 626 5. Owen, D. J. & Evans, P. R. A Structural Explanation for the Recognition of
627 Tyrosine-Based Endocytotic Signals. *Science (80-.).* **282**, 1327–1332 (1998).
- 628 6. Höning, S. *et al.* Phosphatidylinositol-(4,5)-Bisphosphate Regulates Sorting
629 Signal Recognition by the Clathrin-Associated Adaptor Complex AP2. *Mol. Cell*
630 **18**, 519–531 (2005).
- 631 7. Kelly, B. T. *et al.* A structural explanation for the binding of endocytic dileucine
632 motifs by the AP2 complex. *Nature* **456**, 976–979 (2008).
- 633 8. Hardy, G. J., Nayak, R. & Zauscher, S. Model cell membranes: Techniques to
634 form complex biomimetic supported lipid bilayers via vesicle fusion. *Curr. Opin.*
635 *Colloid Interface Sci.* **18**, 448–458 (2013).
- 636 9. Clifton, L. A. *et al.* Design and use of model membranes to study biomolecular
637 interactions using complementary surface-sensitive techniques. *Adv. Colloid*
638 *Interface Sci.* **277**, 102118 (2020).
- 639 10. Eeman, M. & Deleu, M. From biological membranes to biomimetic model
640 membranes. *Biotechnology, Agronomy and Society and Environment* vol. 14
641 719–736 (2010).
- 642 11. Richter, R. P., Bérat, R. & Brisson, A. R. Formation of Solid-Supported Lipid
643 Bilayers: An Integrated View. *Langmuir* **22**, 3497–3505 (2006).

- 644 12. Viitala, T., Hautala, J. T., Vuorinen, J. & Wiedmer, S. K. Structure of Anionic
645 Phospholipid Coatings on Silica by Dissipative Quartz Crystal Microbalance.
646 *Langmuir* **23**, 609–618 (2007).
- 647 13. Anderson, T. H. *et al.* Formation of Supported Bilayers on Silica Substrates.
648 *Langmuir* **25**, 6997–7005 (2009).
- 649 14. Seantier, B. & Kasemo, B. Influence of Mono- And Divalent Ions on the
650 Formation of Supported Phospholipid Bilayers via Vesicle Adsorption. *Langmuir*
651 **25**, 5767–5772 (2009).
- 652 15. Dacic, M. *et al.* Influence of Divalent Cations on Deformation and Rupture of
653 Adsorbed Lipid Vesicles. *Langmuir* **32**, 6486–6495 (2016).
- 654 16. Kunze, A., Zhao, F., Marel, A.-K., Svedhem, S. & Kasemo, B. Ion-mediated
655 changes of supported lipid bilayers and their coupling to the substrate. A case of
656 bilayer slip? *Soft Matter* **7**, 8582–8591 (2011).
- 657 17. Reimhult, E., Höök, F. & Kasemo, B. Temperature dependence of formation of a
658 supported phospholipid bilayer from vesicles on SiO₂. *Phys. Rev. E - Stat.*
659 *Physics, Plasmas, Fluids, Relat. Interdiscip. Top.* **66**, 4 (2002).
- 660 18. Meker, S., Chin, H., Sut, T. N. & Cho, N.-J. Amyloid- β Peptide Triggers
661 Membrane Remodeling in Supported Lipid Bilayers Depending on Their
662 Hydrophobic Thickness. *Langmuir* **34**, 9548–9560 (2018).
- 663 19. Satriano, C. *et al.* Ferritin-supported lipid bilayers for triggering the endothelial
664 cell response. *Colloids Surfaces B Biointerfaces* **149**, 48–55 (2017).
- 665 20. Fan, X. *et al.* Lipid-mimicking peptide decorates erythrocyte membrane for active
666 delivery to engrafted MDA-MB-231 breast tumour. *Eur. J. Pharm. Biopharm.*
667 **152**, 72–84 (2020).
- 668 21. Bailey-Hytholt, C. M., Puranik, T., Tripathi, A. & Shukla, A. Investigating
669 interactions of phthalate environmental toxicants with lipid structures. *Colloids*
670 *Surfaces B Biointerfaces* **190**, 110923 (2020).
- 671 22. Montis, C. *et al.* Nucleolipid bilayers: A quartz crystal microbalance and neutron

- 672 reflectometry study. *Colloids Surfaces B Biointerfaces* **137**, 203–213 (2016).
- 673 23. Woller, J. G., Börjesson, K., Svedhem, S. & Albinsson, B. Reversible
674 Hybridization of DNA Anchored to a Lipid Membrane via Porphyrin. *Langmuir* **28**,
675 1944–1953 (2012).
- 676 24. Fragneto, G., Delhom, R., Joly, L. & Scoppola, E. Neutrons and model
677 membranes: Moving towards complexity. *Curr. Opin. Colloid Interface Sci.* **38**,
678 108–121 (2018).
- 679 25. F. Dufrêne, Y., Boland, T., W. Schneider, J., R. Barger, W. & U. Lee, G.
680 Characterization of the physical properties of model biomembranes at the
681 nanometer scale with the atomic force microscope. *Faraday Discuss.* **111**, 79–
682 94 (1999).
- 683 26. Ellenbroek, W. G. *et al.* Divalent Cation-Dependent Formation of Electrostatic
684 PIP2 Clusters in Lipid Monolayers. *Biophys. J.* **101**, 2178–2184 (2011).
- 685 27. Wang, Y.-H. *et al.* Divalent Cation-Induced Cluster Formation by
686 Polyphosphoinositides in Model Membranes. *J. Am. Chem. Soc.* **134**, 3387–
687 3395 (2012).
- 688 28. Bilkova, E. *et al.* Calcium Directly Regulates Phosphatidylinositol 4,5-
689 Bisphosphate Headgroup Conformation and Recognition. *J. Am. Chem. Soc.*
690 **139**, 4019–4024 (2017).
- 691 29. Luchini, A. *et al.* Towards biomimics of cell membranes: Structural effect of
692 phosphatidylinositol triphosphate (PIP3) on a lipid bilayer. *Colloids Surfaces B*
693 *Biointerfaces* **173**, 202–209 (2019).
- 694 30. Jouhet, J. Importance of the hexagonal lipid phase in biological membrane
695 organization. *Frontiers in Plant Science* vol. 4 (2013).
- 696 31. Lind, T. K., Skoda, M. W. A. & Cárdenas, M. Formation and Characterization of
697 Supported Lipid Bilayers Composed of Phosphatidylethanolamine and
698 Phosphatidylglycerol by Vesicle Fusion, a Simple but Relevant Model for
699 Bacterial Membranes. *ACS Omega* **4**, 10687–10694 (2019).

- 700 32. Howland, M. C., Szmodis, A. W., Sanii, B. & Parikh, A. N. Characterization of
701 Physical Properties of Supported Phospholipid Membranes Using Imaging
702 Ellipsometry at Optical Wavelengths. *Biophys. J.* **92**, 1306–1317 (2007).
- 703 33. N'Diaye, M., Michel, J.-P. & Rosilio, V. Relevance of charges and polymer
704 mechanical stiffness in the mechanism and kinetics of formation of
705 liponanoparticles probed by the supported bilayer model approach. *Phys. Chem.*
706 *Chem. Phys.* **21**, 4306–4319 (2019).
- 707 34. Voinova, M. V, Rodahl, M., Jonson, M. & Kasemo, B. Viscoelastic Acoustic
708 Response of Layered Polymer Films at Fluid-Solid Interfaces: Continuum
709 Mechanics Approach. *Phys. Scr.* **59**, 391–396 (1999).
- 710 35. Sauerbrey, G. Verwendung von Schwingquarzen zur Wägung dünner Schichten
711 und zur Mikrowägung. *Zeitschrift für Phys.* **155**, 206–222 (1959).
- 712 36. Dixon, M. C. Quartz crystal microbalance with dissipation monitoring: enabling
713 real-time characterization of biological materials and their interactions. *J. Biomol.*
714 *Tech.* **19**, 151–158 (2008).
- 715 37. Easley, A. D. *et al.* A practical guide to quartz crystal microbalance with
716 dissipation monitoring of thin polymer films. *J. Polym. Sci.* **60**, 1090–1107
717 (2022).
- 718 38. Cho, N.-J., Kanazawa, K. K., Glenn, J. S. & Frank, C. W. Employing Two
719 Different Quartz Crystal Microbalance Models To Study Changes in Viscoelastic
720 Behavior upon Transformation of Lipid Vesicles to a Bilayer on a Gold Surface.
721 *Anal. Chem.* **79**, 7027–7035 (2007).
- 722 39. Pan, J., Tristram-Nagle, S., Kučerka, N. & Nagle, J. F. Temperature
723 Dependence of Structure, Bending Rigidity, and Bilayer Interactions of
724 Dioleoylphosphatidylcholine Bilayers. *Biophys. J.* **94**, 117–124 (2008).
- 725 40. Gallová, J., Uhríková, D., Islamov, A., Kuklin, A. & Balgavý, P. Effect of
726 cholesterol on the bilayer thickness in unilamellar extruded DLPC and DOPC
727 liposomes: SANS contrast variation study. *Gen. Physiol. Biophys.* **23**, 113–128

- 728 (2004).
- 729 41. Leonenko, Z. V, Finot, E., Ma, H., Dahms, T. E. S. & Cramb, D. T. Investigation
730 of Temperature-Induced Phase Transitions in DOPC and DPPC Phospholipid
731 Bilayers Using Temperature-Controlled Scanning Force Microscopy. *Biophys. J.*
732 **86**, 3783–3793 (2004).
- 733 42. Attwood, S. J., Choi, Y. & Leonenko, Z. Preparation of DOPC and DPPC
734 Supported Planar Lipid Bilayers for Atomic Force Microscopy and Atomic Force
735 Spectroscopy. *International Journal of Molecular Sciences* vol. 14 3514–3539
736 (2013).
- 737 43. Orsi, M., Michel, J. & Essex, J. W. Coarse-grain modelling of DMPC and DOPC
738 lipid bilayers. *J. Phys. Condens. Matter* **22**, 155106 (2010).
- 739 44. Maestro, A. & Gutfreund, P. In situ determination of the structure and
740 composition of Langmuir monolayers at the air/water interface by neutron and X-
741 ray reflectivity and ellipsometry. *Adv. Colloid Interface Sci.* **293**, 102434 (2021).
- 742 45. Santamaria, A. *et al.* Strikingly Different Roles of SARS-CoV-2 Fusion Peptides
743 Uncovered by Neutron Scattering. *J. Am. Chem. Soc.* **144**, 2968–2979 (2022).
- 744 46. Carrascosa-Tejedor, J., Santamaria, A., Pereira, D. & Maestro, A. Structure of
745 DPPC Monolayers at the Air/Buffer Interface: A Neutron Reflectometry and
746 Ellipsometry Study. *Coatings* vol. 10 (2020).
- 747 47. Bechinger, B. DNP Solid-State NMR of Biological Membranes. *eMagRes* 25–34
748 (2018) doi:doi:10.1002/9780470034590.emrstm1558.
- 749 48. van der Wel, P. C. A. New applications of solid-state NMR in structural biology.
750 *Emerg. Top. life Sci.* **2**, 57–67 (2018).
- 751 49. Höök, F. & Kasemo, B. The QCM-D Technique for Probing Biomacromolecular
752 Recognition Reactions BT - Piezoelectric Sensors. in (eds. Janshoff, A. &
753 Steinem, C.) 425–447 (Springer Berlin Heidelberg, 2007). doi:10.1007/978-3-
754 540-36568-6_12.
- 755 50. Liu, G. & Zhang, G. Basic Principles of QCM-D. in (eds. Liu, G. & Zhang, G.) 1–8

- 756 (Springer Berlin Heidelberg, 2013). doi:10.1007/978-3-642-39790-5_1.
- 757 51. Cubitt, R. & Fragneto, G. D17: the new reflectometer at the ILL. *Appl. Phys. A*
758 **74**, s329–s331 (2002).
- 759 52. Gutfreund, P. *et al.* Towards generalized data reduction on a chopper-based
760 time-of-flight neutron reflectometer. *J. Appl. Crystallogr.* **51**, 606–615 (2018).
- 761 53. Nelson, A. Co-refinement of multiple-contrast neutron/X-ray reflectivity data
762 using MOTOFIT. *J. Appl. Crystallogr.* **39**, 273–276 (2006).
- 763